


Spatial characteristics of a zero-pressure-gradient turbulent boundary layer in the presence of free-stream turbulence

Eda Dogan ^{1,2,*} R. Jason Hearst,^{3,2} Ronald E. Hanson,^{4,2} and Bharathram Ganapathisubramani²

¹Linné FLOW Centre, KTH Mechanics, Stockholm, SE-100 44, Sweden

²Engineering and the Environment, University of Southampton, Southampton, SO17 1BJ, United Kingdom

³Department of Energy and Process Engineering, Norwegian University of Science and Technology, Trondheim, NO-7491, Norway

⁴Department of Mechanical Engineering, York University, Toronto, Ontario M3J 1P3, Canada



(Received 24 July 2018; published 1 August 2019)

Particle image velocimetry (PIV) measurements are performed to examine the structural organization inside a turbulent boundary layer under the influence of free-stream turbulence (FST). In particular, streamwise-wall-normal plane PIV measurements are presented for two cases at two different turbulent intensity levels (about 13% and 8%). The free-stream turbulence is generated using an active grid in a wind tunnel. The statistical information of the flow regarding the wall-normal velocity and Reynolds shear stress are presented. The effect of increasing the turbulence level in the free stream for these flows has been found to have similarities with increasing Reynolds number for high-Reynolds-number canonical flows. Quadrant analysis is performed to determine the contributions of different Reynolds-stress-producing events. In this regard, the distribution of momentum transport events shows some similarity with channel flows, which can be justified by comparison of similar intermittency characteristics of both flows. In addition, the coherent structures found inside the boundary layer have inclined features that are consistent with the previous studies for canonical flows. The fact that the external disturbance, such as FST in this study, does not alter the organization of the structures inside the boundary layer supports the growing evidence for a universal structure for wall-bounded flows.

DOI: [10.1103/PhysRevFluids.4.084601](https://doi.org/10.1103/PhysRevFluids.4.084601)

I. INTRODUCTION

In many naturally occurring flows or in flows of industrial significance, boundary layers are often subjected to the external influence of free-stream turbulence (FST). Examples of the effects of FST on turbulent boundary layers include enhanced heat transfer and increased skin friction [1,2], which can be both beneficial and detrimental on the performance of an engineering device. FST penetrates into the boundary layer, which affects the momentum and energy transport within through interactions between those turbulent scales imparted by FST and those occurring naturally inside the boundary layer. FST is also known to play a critical role in boundary layer transition mechanisms; see, for example, Hunt *et al.* [3]. More recently, the analysis of the effects of FST penetration inside turbulent boundary layers are considered by Sharp *et al.* [4] and Dogan *et al.* [5,6] in terms of scale interactions. Sharp *et al.* [4] found similarities in energy distributions inside the boundary layer to the ones occurring in canonical turbulent boundary layers at similar Re_τ , which is the friction-velocity-based Reynolds number defined as $U_\tau \delta / \nu$ where U_τ is the friction velocity, δ is the boundary layer thickness, and ν is the kinematic viscosity. Dogan *et al.* [5,6] expanded upon this observation by

*eda.dogan@mech.kth.se

examining the near-wall turbulence statistics that were obtained using single-component hot-wire anemometry. It was shown that the large-scale structures occurring in the free stream penetrate into the boundary layer and modulate the small-scale structures occurring in the near-wall region. The modulation effect became more prominent with increasing level of FST, which was found to be analogous to the effect of increasing Re_τ in high-Reynolds-number flows. The analogy between turbulent boundary layer having high levels of FST at moderate Re and high- Re in the absence of any appreciable levels of FST is based on the observation that large energetic motions in the outer region in boundary layers, known as superstructures, become more energetic, and their footprint in the near-wall region becomes more important with increasing Re_τ . These superstructures carry a significant portion of the turbulent kinetic energy, contributing to nearly half the Reynolds stresses in these flows [7–9].

The turbulence-producing events in a canonical boundary layer include “ejections” as low-speed fluid close to the wall is pushed away from the wall and “sweeps” as high-speed fluid is moved towards the wall. For boundary layers under the influence of FST, very limited information is available on multicomponent velocity measurements. Two-velocity-component information is available either by cross-wire measurements [2,4,10,11] or laser doppler anemometry (LDV) [12]. In the aforementioned studies, turbulence statistics were considered in terms of the mean Reynolds shear stress and the mean and rms of the velocity fluctuations. However, little information on the spatial structure of the turbulent flow exists for this scenario. The objective of the present research is to address this through detailed spatial correlation information in a turbulent boundary layer subjected to FST.

In this experimental study, planar particle image velocimetry (PIV) measurements are performed to examine the spatial structure as well as the momentum transport events in boundary layers under the influence of FST. In particular, streamwise-wall-normal plane PIV measurements will be presented for two cases at two different turbulence intensity levels: one having approximately 8% and another approximately 13% of free-stream turbulence intensity levels. The distribution of the velocity fluctuations in the context of the momentum flux events will be discussed in detail. Finally, length scales and coherence in the flow obtained using the two-point correlations will also be discussed.

II. EXPERIMENTAL PROCEDURE

The experiments were performed in an open-circuit suction-type wind tunnel at the University of Southampton. The tunnel has a $0.9 \times 0.6 \times 4.5$ m cross section, and a turbulent boundary layer was established on a suspended floor. Free-stream turbulence was generated with an active grid. This grid contains eleven vertical and seven horizontal rod arrays that have wings attached on them and can be independently controlled by stepper motors and is based on the original design by Makita [13]. Detailed information on the facility and active grid design are found in Dogan *et al.* [5].

Measurements of the streamwise and wall-normal flow velocity in the boundary layer and in the free stream were made using planar PIV in the present study to enable analysis of the instantaneous and ensemble-averaged spatial features of the turbulent boundary layer in the presence of FST. An arrangement of three cameras was used to image the measurement plane. The three LaVision ImagerProLX CCD 16 megapixel cameras were fitted with Nikon Nikkor lenses having a focal length of 200 mm at an f-stop (aperture) of 8. The cameras were oriented in a T-shaped formation to acquire both the boundary layer and the free stream with a field of view of each camera overlapping by 1 cm. The leading edge of the measurement plane is approximately 3.2 m downstream of the midplane of the active grid. The field of view was approximately 32 cm by 27 cm in the streamwise and wall-normal directions, respectively. The laser sheet was generated by a Litron Lasers Nano L200 15PIV Nd:YAG laser (532 nm wavelength, 200 mJ/pulse, 15 Hz repetition rate) and illuminated a streamwise-wall-normal plane perpendicular to the test plate. The experimental arrangement described, with an example flow field using the T-shaped arrangement of cameras, is demonstrated in Fig. 1. The time delay between laser pulses was chosen as $70 \mu\text{s}$

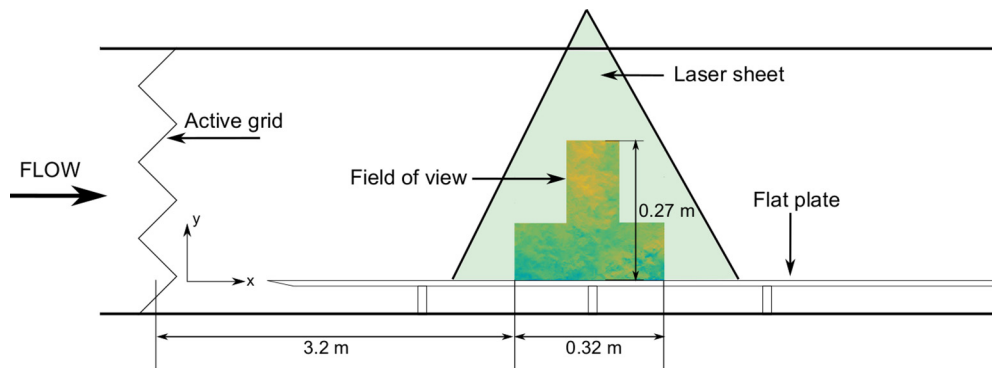


FIG. 1. Schematic of the test section with illuminated field of view (not to scale).

to optimize the accuracy of the measurements. The flow was seeded with particles of a glycol and demineralized water solution. In total, 2000 image pairs were acquired and then were processed with LaVision DaVis 8.2.2. Owing to the large measurement region of interest, and the known adverse effect of pixel locking [14], the potential effects were mitigated using the algorithm developed by Hearst and Ganapathisubramani [15]. The application of this method is as follows. The images were preprocessed by first applying a sliding background subtraction filter to reduce noise, and then applying a 3×3 Gaussian kernel filter to slightly blur the particles over more pixels; the latter helps to reduce the influence of pixel locking. The vector fields were then computed using 50% overlap and five passes reducing from $96 \text{ pixels} \times 96 \text{ pixels}$ windows to $16 \text{ pixels} \times 16 \text{ pixels}$ windows. Window deformation was used on final passes to mitigate pixel locking. Finally, the vectors were postprocessed by applying histogram equalization on a vector-by-vector basis as described by Hearst and Ganapathisubramani [15] to further diminish the influence of pixel locking.

III. FLOW CONDITIONS AND BOUNDARY LAYER STATISTICS

In this study, two representative FST cases, B and D, from Dogan *et al.* [5], are considered. Case D is an example of high FST, whereas case B is an example of low FST. The naming convention is retained for consistency. It should be noted that the FST levels in both cases (about 13% and 8%, respectively, for high and low) are still significantly higher than most previous studies that have examined the effects of FST. The active grid protocol for each case is reproduced from Larssen and Devenport [16] from their test case 14. These two cases differ only by their blockage ratio depending on which wings were used, either solid wings or cutout wings with holes. This will generate a free-stream turbulence with similar length scales and isotropy but with different turbulence intensity levels [17]. The most energetic scales generated in the free stream for these two flows are reported to be similar in Dogan *et al.* [5], i.e., as large as 10 times the corresponding boundary layer thickness. This gives a solid basis to isolate the effects of free-stream turbulence level on the spatial organization of the two flows. For the present PIV results, values of the skin friction velocity were obtained by Preston tube measurements as reported in Dogan *et al.* [5]. Oil film interferometry was later applied to validate the Preston-tube estimates of skin-friction values [18].

A comparison of the mean and variance of streamwise velocity from PIV and the previously reported hot-wire measurements from Dogan *et al.* [5] for the test cases are provided in Fig. 2. For these two set of measurements, the mean velocity and the turbulence intensity in the free stream are matched within less than 3%. In addition to the data by the authors, some reference data from canonical boundary layers and a channel flow are also plotted for comparison. The experimental data are from the canonical boundary layer at $Re_\tau = 7300$ by Hutchins and Marusic [19] and at $Re_\tau = 15000$ by Talluru *et al.* [20]. The direct numerical simulation (DNS) data are for a channel flow at $Re_\tau = 5200$ by Lee and Moser [21]. The superscript + is used to denote the inner scaling of

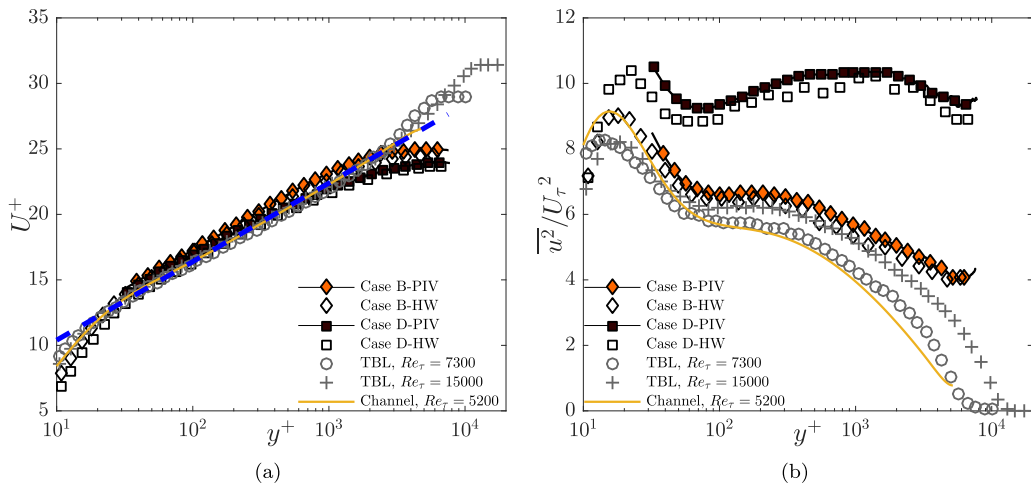


FIG. 2. (a) Mean and (b) variance profiles of the streamwise velocity component in inner scaling from the present PIV measurements and hot-wire measurements from Dogan *et al.* [5]. Canonical cases from the literature are included for comparison. Dashed line in panel (a) is the log law with coefficients $\kappa = 0.384$ and $B = 4.4$. Markers on the PIV data curve are undersampled for clarity.

length (normalized by ν/U_τ) and velocity (normalized by U_τ). The convention throughout the paper is that the capital letter for velocity is given for its mean value, whereas the lower case refers to its fluctuating component. Although the near-wall statistics are resolved with high resolution only for the hot-wire measurements, the close resemblance between the two profiles throughout the rest of the boundary layer provides confidence in the current measurements. The mean profiles in Fig. 2(a) show a distinctly suppressed wake region and an extended logarithmic region with the log-law coefficients $\kappa = 0.384$ and $B = 4.4$, and this observation is further exemplified in comparison to the various canonical reference cases. The mean profiles for the boundary layers subjected to FST resemble channel flows as discussed in Dogan *et al.* [5] due to similar intermittency characteristics. The variance profiles [Fig. 2(b)] show two main features for FST cases. One feature is that the amplitude of the near-wall peak increases with FST level. Another feature is the amplification of the fluctuations in the outer region of the boundary layer. Each of the observed features is caused by the increased turbulence level in the free stream. When compared to the profiles for canonical boundary layers and channel flow, the observed changes in the mean flow and turbulent fluctuations are consistent with the effect of increasing Reynolds number, which is clearly demonstrated in the outer region. In the near-wall region, the wire resolution for high Re case may not be sufficient to resolve the small scales and may therefore not accurately capture the change in the amplitude of the near-wall peak. Nevertheless, the consistency of the outer region profile for FST case B and the highest Re case is remarkable. The effect of increasing FST level and increasing Reynolds number has a similar influence on the large scales in the outer region and on the near-wall region. A detailed discussion of these observations is given by Dogan *et al.* [5].

A summary of the various flow parameters of the two FST cases considered are given in Table I. The subscript “0” is used to denote parameters calculated from the free stream. The boundary layer thickness, δ , from PIV measurements is defined as the height at which the mean turbulence intensity profile is within 1% of the turbulence intensity in the free stream. This method was preferable to the traditional definition of δ_{99} , such as that of Perry and Li [22], where an iterative approach is used to estimate δ_{99} . The latter was found to fail for the PIV data owing to a combination of random uncertainty in the free-stream measurement and insufficient near-wall resolution, which resulted in poor convergence of the integral scheme. The Taylor microscale, λ_0 , corresponding

TABLE I. Free-stream and turbulent boundary layer parameters for the study cases. U_0 : mean streamwise velocity of the free stream, $\sqrt{u_0^2}/U_0$ (%): free-stream turbulence intensity, Re_{λ_0} : Reynolds number based on the free-stream Taylor microscale, δ : boundary-layer thickness, U_τ : friction velocity, Re_τ : Reynolds number based on the friction velocity, Re_θ : Reynolds number based on the momentum thickness.

FST cases	U_0 (m/s)	$\sqrt{u_0^2}/U_0$ (%)	Re_{λ_0}	δ (mm)	θ (mm)	U_τ (m/s)	Re_τ	Re_θ
B (diamond)	10.2	8.1	505	176	6.8	0.41	4640	4330
D (square)	10.1	12.8	645	183	8.0	0.42	4930	5130

Reynolds number, $Re_{\lambda_0} = \sqrt{u_0^2} \lambda_0 / \nu$, and friction velocity, U_τ , are from Dogan *et al.* [5], where these parameters were determined from measurements made using a single hot-wire probe and Preston tube, respectively.

A. Wall-normal velocity

The inner and outer scaled mean wall-normal velocity profiles are shown in Fig. 3. The ability for inner scaling [Fig. 3(a)] to result in near-wall similarity is significant since it suggests that the effect of the turbulence level in the free stream results in a comparable increase in the skin friction, U_τ . However, past $y^+ > 100$, this collapse is no longer evident, which aligns with the mid-log region where FST occurs due to direct penetration. Considering Fig. 3, the case having a higher turbulence level in the free stream results in an increase in the mean wall-normal velocity component.

Recently an outer scaling method was proposed for the mean wall-normal velocity component by Wei and Klewicki [23]. This scaling of the mean wall-normal velocity by the mean wall-normal velocity in the free stream, V_0 , is reproduced in Fig. 3(b). Some improvement in the similarity is noticeable in the wake and outer region for $y/\delta > 0.1$; however, the results fail to adequately collapse. Regardless, the improved similarity beyond the near-wall region suggests that this scaling may capture the local effects caused by the presence of free-stream turbulence. The combined near-wall and log-region variation gives evidence of more

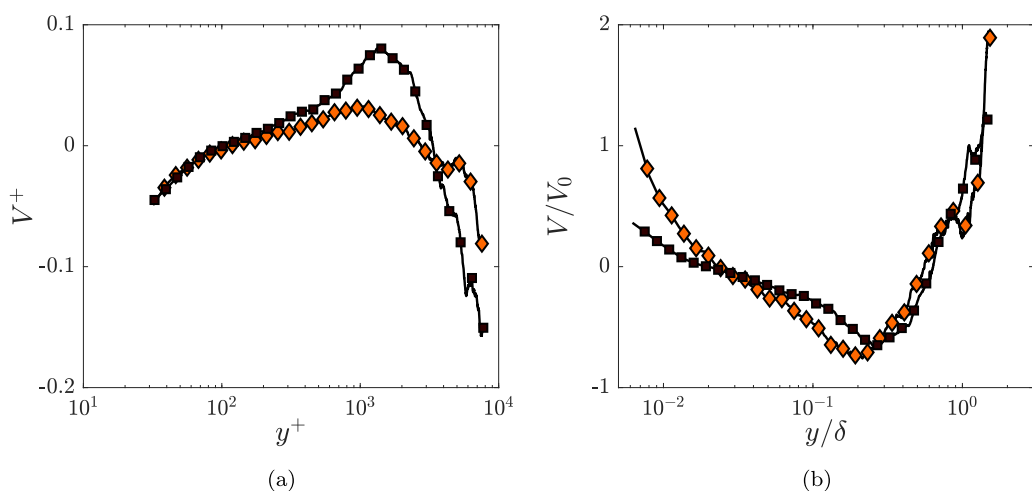


FIG. 3. Mean wall-normal velocity profile in (a) inner scaling, (b) outer scaling as proposed by Wei and Klewicki [23]. Markers on the PIV data curve are undersampled for clarity. Case B: filled diamond, case D: filled square.

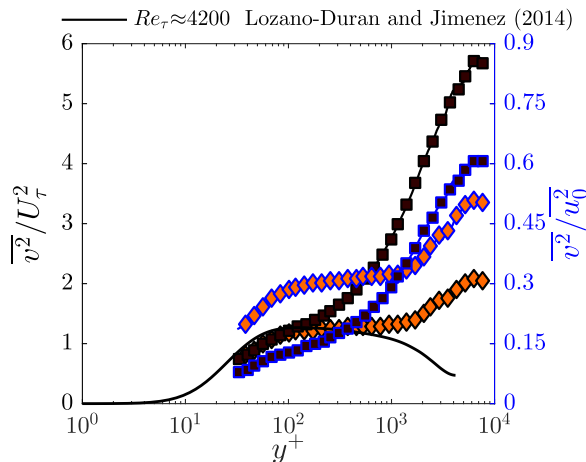


FIG. 4. Variance profiles of the wall-normal velocity fluctuations. The ordinates show the profiles as (left) normalized by inner scaling and (right) normalized by the variance of the free-stream streamwise velocity fluctuations (blue outlined). Markers on the PIV data curve are interpolated data points for clear representation. Case B: filled diamond, case D: filled square.

complex phenomena in these cases. It is possible that the free-stream turbulence and the degree of randomness inflicted by its presence reduces the fidelity of this scaling.

The variance profiles of the wall-normal velocity fluctuations are given in comparison with the channel flow data from Lozano-Durán and Jiménez [24] at a comparable Re_τ in Fig. 4. The similarity between the channel flows and turbulent boundary layers under FST is especially found in the wake region where the intermittency is lost for these two flows, with the presence of a turbulent core in the centerline of the channel and the FST, respectively. As is shown in Fig. 4, the case having a lower FST level more closely follows the corresponding channel flow example, whereas the higher FST case deviates first. The near-wall similarity up to mid-log region is observed. The similarity of the profiles is sustained until the point FST cases peel up with the intense wall-normal fluctuations due to the presence of turbulence in the free stream. It has been shown in the literature for high-Reynolds-number flows that the wall-normal fluctuations exhibit a nearly constant extended plateau [25–27]. The presence of this plateau region again supports the analogy between enhanced FST and high Re number flows.

The distinction between the wall-normal variance profiles of the two FST cases shown in Fig. 4 is pronounced for $y^+ > 200$ and approaching the free stream as expected due to their different free-stream turbulence levels. This suggests that the free-stream turbulence appears to set the skin-friction velocity, and the flow responds proportionally to the increase in skin friction. This may be understood by considering that the integrated momentum flux over the thickness of the boundary layer is related to the drag (i.e., skin friction) of the surface. Therefore, the velocity fluctuations should, in turn, scale with skin-friction velocity. Regardless, the degree of similarity between the three profiles in the inner region is remarkable. The fidelity of this scaling for the momentum flux (i.e., Reynolds shear stress) is also examined in Sec. III B. The right axis of the figure (blue outlined) is given as normalized with the variance of the streamwise velocity fluctuations of the free stream. This would also give information about the isotropy of the flow in the free stream. The isotropy ratio

in the free stream can be defined as $I = \frac{\sqrt{u_0^2}}{\sqrt{v_0^2}}$. The isotropy (or anisotropy thereof) is found to be around 1.4 for case B and around 1.3 for case D. These values are slightly higher than the previous active grid studies that similarly followed Makita’s original active grid design [16,28]. Given that the anisotropy is mostly associated with the largest scales of the flow and since in this study the u

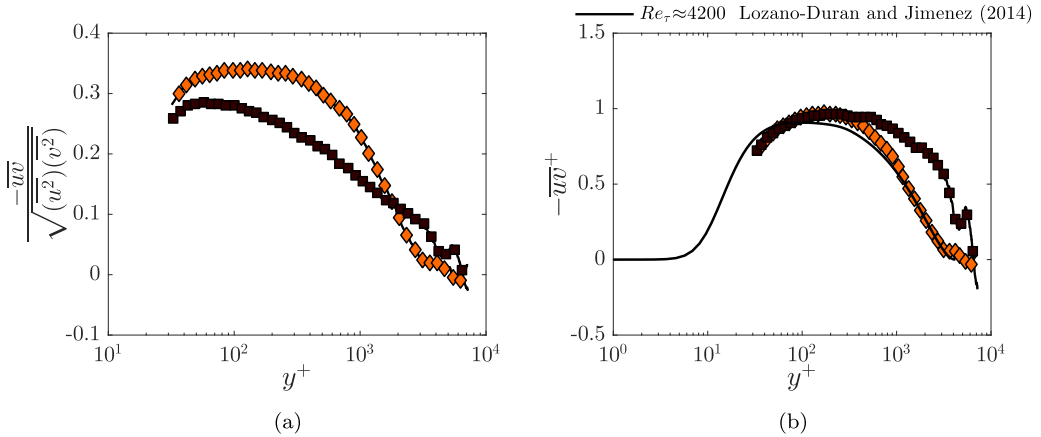


FIG. 5. (a) Shear stress correlation coefficient and (b) inner-normalized Reynolds shear stress profiles. Markers on the PIV data curve are interpolated data points for clear representation. Case B: filled diamond, case D: filled square.

fluctuations are forced to be large scale (such that the spectral peak was at 10δ), the lack of isotropy is expected.

B. Reynolds shear stress profiles

The shear stress correlation coefficient, also known as the velocity correlation coefficient, is shown in Fig. 5(a). As was shown previously, for example, in the variance profiles from Fig. 2(b), the free-stream turbulence penetrates the boundary layer, and higher free-stream turbulence levels correspond to enhanced variance throughout. As is shown in Fig. 5(a), the free-stream turbulence that penetrates the boundary layer further reduces correlations, and the effect is enhanced by the level of FST. A similar effect was also observed by Hancock and Bradshaw [10] and Thole and Bogard [12] for boundary layers subjected to FST. The aforementioned suggested that the uncorrelated large scales from the free stream have only a small contribution to the Reynolds shear stress in the inner region. For canonical flows, this is similarly observed with increasing Reynolds number [25,29]. Priyadarshana and Klewicki [29] showed that at high Reynolds number, the spectral overlap between the u and v signals is reduced, thereby reducing the correlation between the two; however, they did not observe an apparent effect in the Reynolds shear stress. Figure 5(b) shows the profiles of the Reynolds shear stress of the present FST cases, which reaffirms the past observations. The wall-normal distance is scaled with the viscous length scale, whereas the shear stress is normalized by friction velocity. The figure shows, as suggested previously, that although for a higher turbulence case the penetration is higher, the inner-scaled Reynolds shear stress is relatively unaffected near the wall. Also in this figure, the channel flow data from Lozano-Durán and Jiménez [24] are plotted for comparison. It is evident from Fig. 5(b) that the lower FST case considered follows the channel flow data more closely than the higher FST case, where the two curves become distinct beyond $y^+ \approx 300$ – 400 . Once again, despite the large amount of disturbance in the free stream, the momentum flux in the near-wall region appears to scale with local skin-friction velocity regardless of the turbulence intensity in the free stream. This similarity in the near-wall region is consistent with the observations for the vertical component as was shown in Figs. 3(a) and 4. However, this behavior is markedly different from the behavior of the streamwise velocity component where the inner scaling with friction velocity did not collapse the profiles in that region. It is also worth noting that the shear stress profiles exhibit an extended plateau region with increasing turbulence level. This is also similar to observations in high-Reynolds-number canonical flows where the extent of the plateau increases with increasing Re_τ .

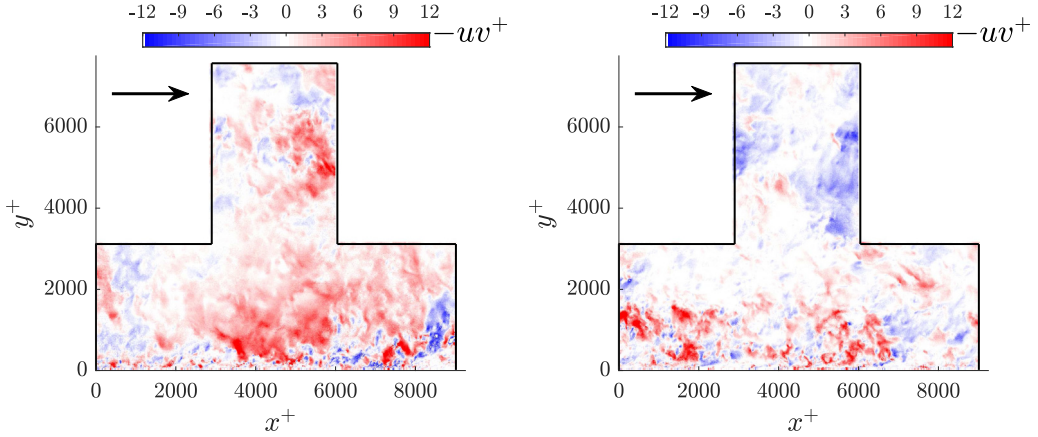


FIG. 6. Contour plot of two snapshots of instantaneous inner-normalized Reynolds shear stress ($-uv^+$) for case B. The enclosed region shows the data from the field of view. Flow is from left to right as indicated by the arrow on top left.

C. Distribution of uv events

Figure 6 shows two snapshots of the instantaneous Reynolds shear stress for a representative FST case. Considerable amount of Reynolds shear stress production can be detected instantaneously from these snapshots, i.e., uv product absolute values as high as $10U_\tau^2$. With the addition of more turbulence in the free stream (case D), the occurrence of uv products beyond $10U_\tau^2$ is even more prominent (not shown). These instantaneous momentum transport events can be characterized by examining the distribution of uv through the boundary layer and comparing against other canonical flows.

In the previous section the ensemble-averaged Reynolds stress was considered. The Reynolds stress can be further decomposed by the probability distribution function (PDF) to compare the distribution of uv events over the boundary layer thickness for each FST case. Figure 7 shows the contour maps of the normalized PDFs of the instantaneous shear stress events for the low FST case B

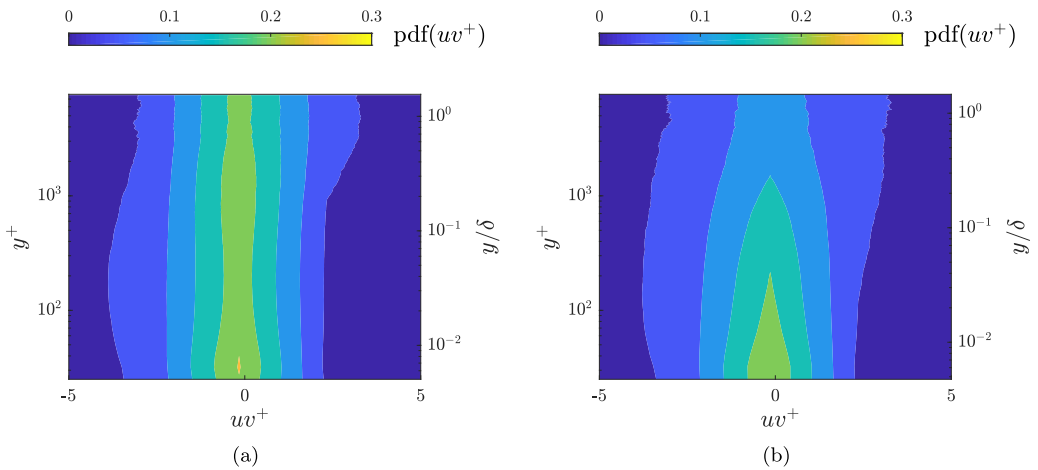


FIG. 7. Contour maps of the normalized PDF of uv . The ordinates show the wall-normal location in inner (left) and outer (right) scaling. (a) Case B, (b) case D.

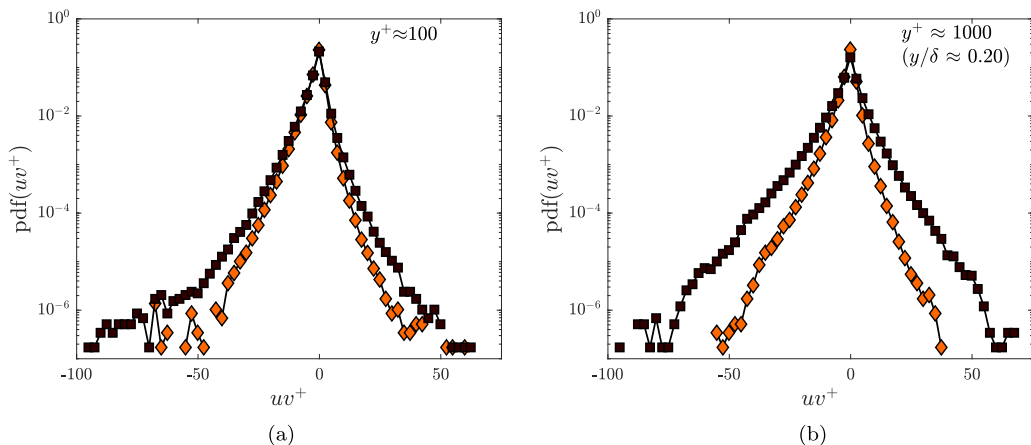


FIG. 8. Comparison of the PDFs of the two FST cases at two wall-normal locations (a) $y^+ \approx 100$ (b) $y/\delta \approx 0.2$. Case B: filled diamond, case D: filled square.

[Fig. 7(a)] and high FST case D [Fig. 7(b)]. From examining Fig. 7, both PDFs appear to be skewed towards negative values, which is consistent with the negative sign of the mean Reynolds shear stress values shown previously in Fig. 5(b). The negatively skewed and also former negative mean values of shear stress events demonstrates that the dominant contributions to total Reynolds stresses are from negative shear stress events of sweeps ($u > 0, v < 0$) and ejections ($u < 0, v > 0$). The negative contributions outweigh the contributions from positive shear stress events of inward ($u < 0, v < 0$) and outward ($u > 0, v > 0$) interactions. It should be noted that the probability of the most intense events is quite low; therefore the colormap of Fig. 7 may not be sufficient to show the differences between the two FST cases. Therefore, profiles can be extracted at various wall-normal locations as done in Fig. 8 to make the distinction clear. At $y^+ \approx 100$, also where the mean Reynolds shear stress showed similarity in Fig. 5(b), the PDFs seem to differ mostly for the intense uv events. This shows the effect of increasing turbulence intensity on the intense ejection and sweep events. Again, this is analogous to an increase in Reynolds number for a canonical wall-bounded flow [30]. For an outer region location, at $y/\delta \approx 0.2$, the higher turbulence case shows an overall distinction in the distribution as also deduced from the mean Reynolds shear stress profile where the two FST cases differ.

At this point of analysis, before moving on to the next section for further discussion of uv events, the normalized PDFs for the normal Reynolds stresses can be compared. Figure 9 presents the PDFs for u^{2+} and v^{2+} for the same wall-normal locations as in Fig. 8. The thickening of the tails of the distributions with increasing turbulence level are more significant for the streamwise normal stresses when compared to wall-normal stress, especially in the logarithmic region. However, the relative importance of the changes between the two FST cases for the streamwise normal stresses and shear stresses is not easily compared between Figs. 8 and 9. This will be further discussed in Sec. IV in relation to shear stress events.

IV. QUADRANT ANALYSIS

The previous analysis showed that (as expected) the probability distribution of uv is skewed towards negative events. To further quantify the uv contributions, the conditional averaging technique of Wallace *et al.* [31] and Lu and Willmarth [32] is applied. They suggested that useful information is contained in the signs of the individual velocity fluctuations. For the conditional averaging technique of Wallace *et al.* [31] and Lu and Willmarth [32], the products of u and v fluctuations are classified by four quadrants of the Reynolds shear stress plane: Q1 ($+u, +v$), Q2 ($-u, +v$),

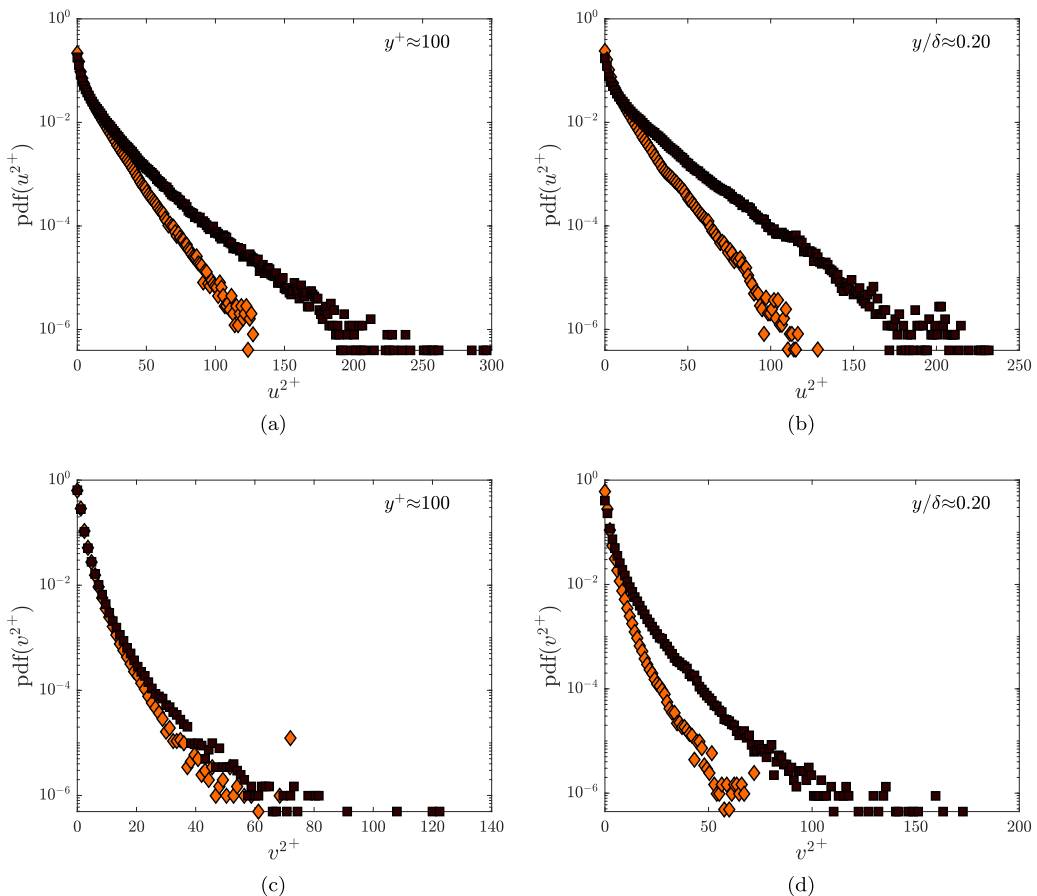


FIG. 9. Comparison of the PDFs of the normal Reynolds stresses for the two FST cases at two wall-normal locations, $y^+ \approx 100$ and $y/\delta \approx 0.2$. Case B: filled diamond, case D: filled square.

Q3 ($-u, -v$), and Q4 ($+u, -v$). Events in the second quadrant, Q2, correspond to negative streamwise fluctuations (low-speed) being lifted away from the wall by positive wall-normal fluctuations, and they are referred to as *ejections*. Events in the fourth quadrant, Q4, correspond to positive streamwise fluctuations (high-speed) being moved towards the wall by negative wall-normal fluctuations, and these motions are called *sweeps*. Q1 and Q3 are called outward and inward interactions, respectively. This type of quadrant analysis does not specify the form of the eddies creating sweeps and ejections, but it permits the analysis of the contribution of these events to the total mean values of various quantities [33].

The Reynolds shear stress can be written as follows:

$$\overline{uv} = \iint_{-\infty}^{\infty} uvP(u, v) du dv, \quad (1)$$

where $P(u, v)$ is the joint PDF and $uvP(u, v)$ is the covariance integrand, i.e., a weighted joint PDF. The integral of the latter distribution over a differential area $du dv$ represents the contribution of that particular pair of u and v to the covariance \overline{uv} in both sign and magnitude. When plotted on the u - v plane, this covariance integrand will be zero on each axis by its definition; therefore, the distribution of contributions to Reynolds shear stress will be distinctly split into four quadrants.

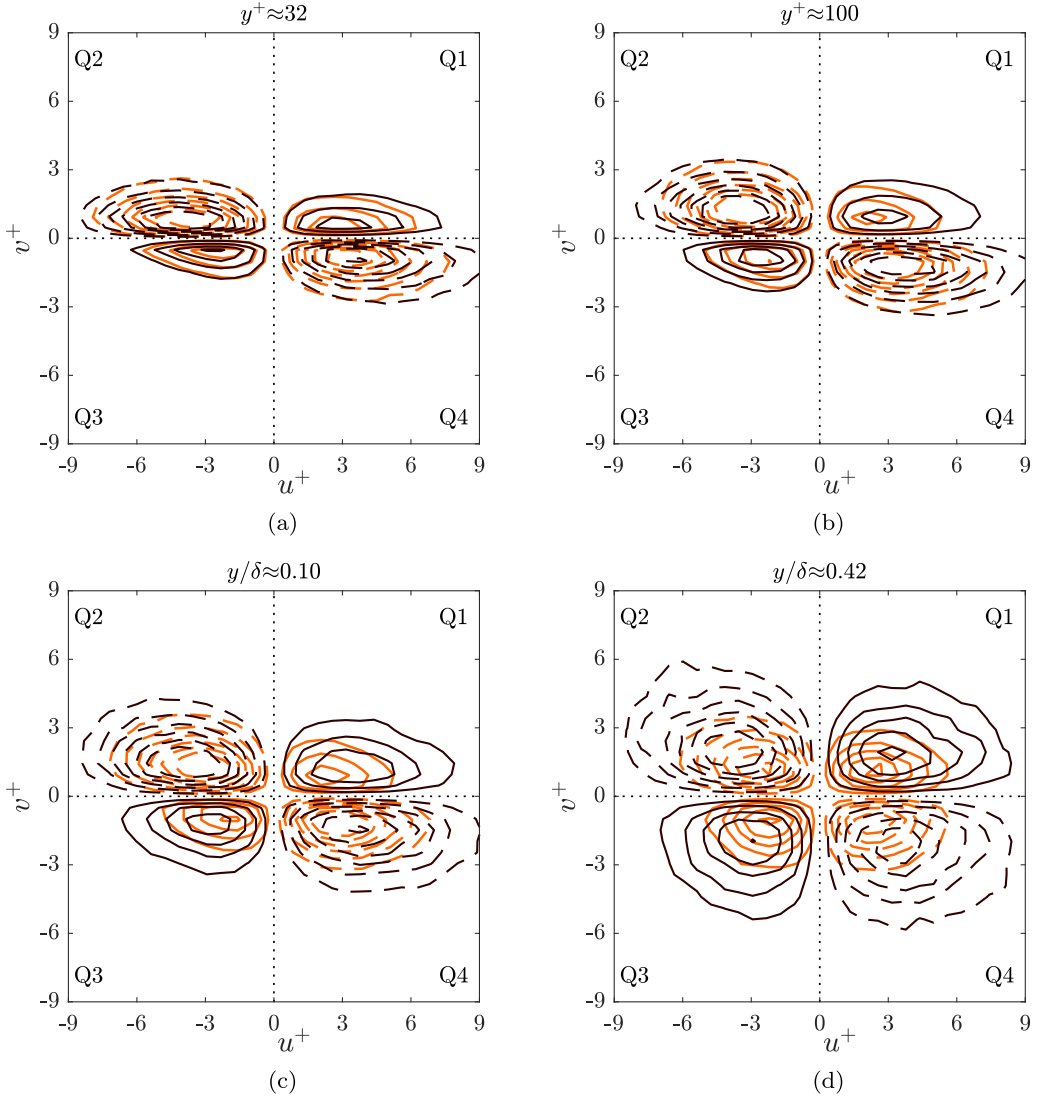


FIG. 10. Covariance integrands of u and v fluctuations for case B (orange) and case D (black) at various wall-normal locations: (a) $y^+ \approx 32$, (b) $y^+ \approx 100$, (c) $y/\delta \approx 0.1$, and (d) $y/\delta \approx 0.42$. Negative contours are shown with dashed lines. The outermost contour level and the increment are 0.01 and 0.01 for positive contours, respectively, and -0.01 and -0.01 for negative contours, respectively. Zero contours are not shown.

Figure 10 shows covariance integrands of u and v at various wall-normal locations for both FST cases. The larger contributions are clearly from Q2 and Q4 events for both cases. In these quadrants, for the high-turbulence case D, the extent of the elliptical shape of the covariance integrand is greater, which shows the effect of increasing turbulence level in the free stream on the intensity of these quadrant events. As the distance from the wall increases towards the free stream, the elliptical shape of the weighted joint PDF becomes more circular and the fractional contributions from Q1 and Q3 events also increase. For a turbulent boundary layer in the absence of FST, the ejections (Q2 events) are known to be dominant above the buffer layer throughout the boundary layer [32,34]. However, for a turbulent boundary layer under the effect of FST, the contribution from sweep events

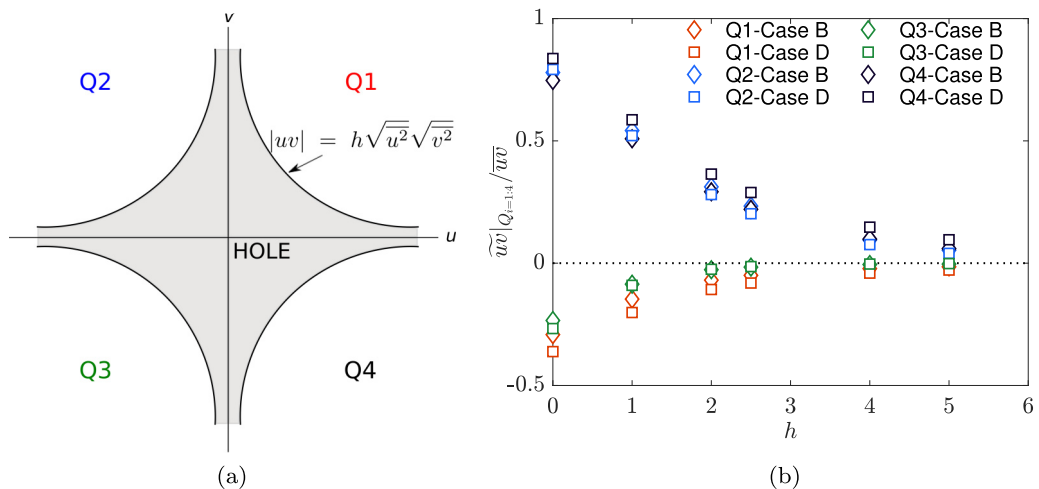


FIG. 11. (a) Schematic illustrating quadrant splitting of the u - v plane with shaded hole region. (b) Fractional contributions to the Reynolds shear stress by each quadrant at $y^+ \approx 40$ for various hole sizes, h , for both FST cases. Symbols are explained in the legend.

is comparable to the contribution from ejections. For case D, the contribution of sweep events is found to exceed the contribution of ejection events, which is supported by the observation of free-stream turbulence penetration into the boundary layer. For example, it is shown in Fig. 3 that there is a greater contribution of negative wall-normal velocity fluctuations for case D with the higher FST level. Comparing the two FST cases, the collapse of the contour maps inside the logarithmic region [Figs. 10(a) and 10(b)] is remarkable, whereas in the outer region [see Figs. 10(c) and 10(d)], the high-intensity FST case shows a broader range of fluctuations that reach larger u and v products, which indicates the direct impact of FST in the outer region.

To focus on the intense occurrences of the Reynolds shear stress, Willmarth and Lu [35] extended the quadrant analysis by introducing a hole filtering. Following their methodology, the u - v plane is divided into five regions as schematically shown in Fig. 11(a). The shaded region in Fig. 11(a) is called “hole” and is bounded by $|uv| = h\sqrt{u^2}\sqrt{v^2}$ where h is a constant. Here a hole size, h , is defined as a threshold to exclude uv events of small magnitude to determine the relative contributions of the more intense uv events. The fractional contributions from each quadrant, Q_i , can be calculated with the relation given below following Lu and Willmarth [32]:

$$\frac{\tilde{uv}|_{Q_i}}{\overline{uv}} = \frac{1}{\overline{uv}} \left[\frac{1}{N} \sum_{n=1}^N uv|_i S_i(h) \right] \quad i = 1:4 \quad (2)$$

where N is the total number of samples, and

$$S_i(h) = \begin{cases} 1, & \text{if } |uv| \geq h\sqrt{u^2}\sqrt{v^2} \text{ and } (u, v) \text{ pair is in the } i\text{th quadrant of the } u\text{-}v \text{ plane,} \\ 0, & \text{otherwise.} \end{cases} \quad (3)$$

Different hole sizes are tested as representatively illustrated for a wall-normal location of $y^+ \approx 40$ in Fig. 11(b). Bogard and Tiederman [36] reported that the optimum threshold for the buffer region is $h \approx 1$, based on direct comparisons between the detected events and instantaneous visualizations of the flow. Lozano-Durán *et al.* [37] were also able to show comparable results for bursts in the buffer region for their threshold value of 1.75. They also observed that their results are qualitatively similar within the range of $1 \leq h \leq 3$. For the present study, the value of h is set at 2, which is located midway in the aforementioned range.

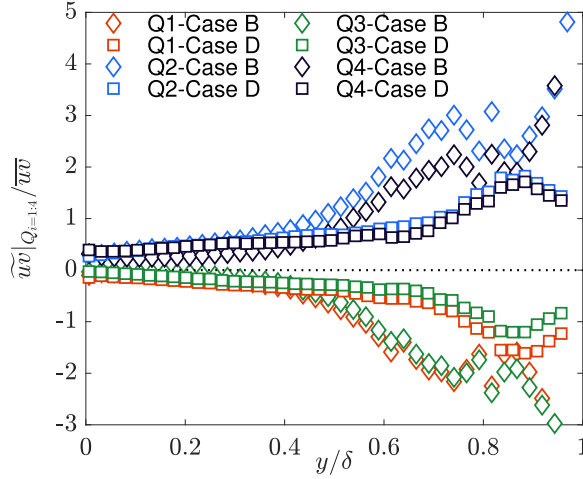


FIG. 12. Distribution of quadrant contributions based on the hole size of $h = 2$ for both FST cases. Symbols are explained in the legend.

Figure 12 presents quadrant contributions with a hole size of $h = 2$ for both cases of FST. When the ratio between the two cases for each quadrant contribution is compared based on this figure (not documented here), it is observed that the effect of increasing FST level is not uniform and it is different for each quadrant. However, it is obvious that the dominant contributors are Q2 and Q4 events for both cases. The outward and inward interactions, Q1 and Q3, respectively, contribute very little to the total Reynolds shear stress. The Q1 and Q3 events have been observed to be more active towards the edge of the boundary layer in the presence of FST as opposed to a canonical turbulent boundary layer. The increased activity of Q1 and Q3 events towards the edge of the boundary layer is similarly found in channel flows as the increased contribution of the two dominant quadrants, Q2 and Q4, near the centerline of the channel is compensated by a parallel increase of the contributions from the quadrants Q1 and Q3 [34]. This similarity can be justified by common intermittency characteristics of the two flows, i.e., channel flow and the turbulent boundary layer under the FST effect. Sweeps are slightly more dominant for high-turbulence case D than low-turbulence case B up to $y/\delta \approx 0.5$, which could be explained by stronger penetration of FST for case D. The contributions from sweeps and ejections for case D seem to be almost equal across the boundary layer. For case B, the ejections seem to be the main contributor to the Reynolds shear stress, and it shows that the near-wall fluctuations are still dominant in their own right for this case.

In Fig. 13(a) the results of Fig. 12 for Q2 and Q4 events are included separately for two cases leading to the discussion for the ratio of Q2 to Q4 events given in Fig. 13(b). Ejections appear to be dominant for the majority of the boundary layer for low-turbulence-level case B. On the other hand, for case D, sweeps are dominant up to $y/\delta \approx 0.1$ from which ejections take over. It is also interesting to note that the ratio of Q2/Q4 exhibits higher values for low-turbulence case B than high-turbulence case D. It is possible that, for case B, the near-wall ejections did not encounter as strong suppression from sweeps towards the wall as it is for case D. This also reveals the robustness of near-wall ejections despite high free-stream fluctuations for both cases. The ratio of Q2/Q4 stays in the range 1.5–2 for channel flows and reaches 3 for a canonical boundary layer at $y \approx \delta$ [34]. For the present study, this ratio is more similar to that of channel flows, over the values observed for canonical turbulent boundary layer flows, although the ratio seems to be justified more by the increased ejections for the present cases as compared to the channel flows [34].

Quadrant analysis is useful to quantify the distributions of the events associated with the high- and low-speed fluid motions. However, it does not directly provide an indication of the spatial scales that contribute to these events. Velocity correlations can provide a great deal of insight of the spatial

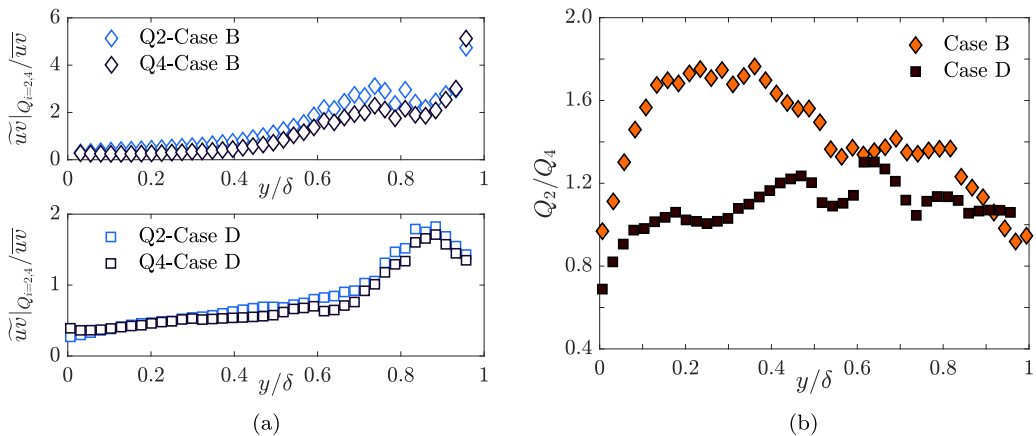


FIG. 13. (a) Figure 12 replotted showing only Q2 and Q4 events for cases B and D, separately. (b) Distribution of the ratio Q2/Q4. Symbols are explained in the legend.

distribution of how these high- and low-speed fluid regions manifest in the flow. For this purpose, the focus of the next section is on the two-point spatial correlations.

V. VELOCITY CORRELATIONS

To provide an estimate of the dimensions of the scales that are involved in generating Reynolds shear stress and in creating the coherent motions of sweeps and ejections, two-point correlations are useful. In a shear flow, when the variable measurement location is displaced throughout the flow relative to a fixed measurement location, the shape and extent of the iso-correlation contours reveal information about the shape and size of the flow structures underlying the correlation [38]. The streamwise-wall-normal plane spatial correlations can be computed using planar PIV data. The two-point correlation coefficient between any two quantities, R_{AB} , is defined as [39]

$$R_{AB} = \frac{\overline{A(x, y)B(x + \Delta x, y + \Delta y)}}{\sigma_A \sigma_B}, \quad (4)$$

where σ_A and σ_B are the standard deviations of A and B, respectively, and Δx and Δy are the streamwise and wall-normal spatial separations, respectively. Multiple realizations are ensemble averaged to obtain the correlation coefficient, which is denoted by an overline. Velocity correlations are computed at each wall-normal location in relation to every other location in the boundary layer. Figure 14 shows the two-point autocorrelations for the streamwise velocity fluctuations, R_{uu} , computed at different wall-normal locations for both cases. Note the abscissa shows the streamwise distance in both the upstream and downstream distance.

In the near-wall [Fig. 14(a)], the contour lines are confined to a relatively small region. As the reference wall-normal location for the correlation calculations moves away from the wall, i.e., in the log layer and above [Figs. 14(b) and 14(e)], the contour lines are more elongated and cover an extended region as similarly observed in canonical flows (Refs. [39,40] among many others). Correlation contours weaker than 0.1 are not shown on the figure; however, it has been noticed that the outer layer is physically connected to every other layer of the boundary layer down to the wall, albeit weakly correlated. This shows the coherence of the structures inside the boundary layer even in the presence of FST. The negative correlations appear to be stronger and more elongated at higher wall-normal locations in the boundary layer. The wall-normal extent of these negatively correlated structures is observed to significantly increase above the log region [Fig. 14(e)]. The field of view of the present measurements is too short to capture the entire extent of these elongated structures. The

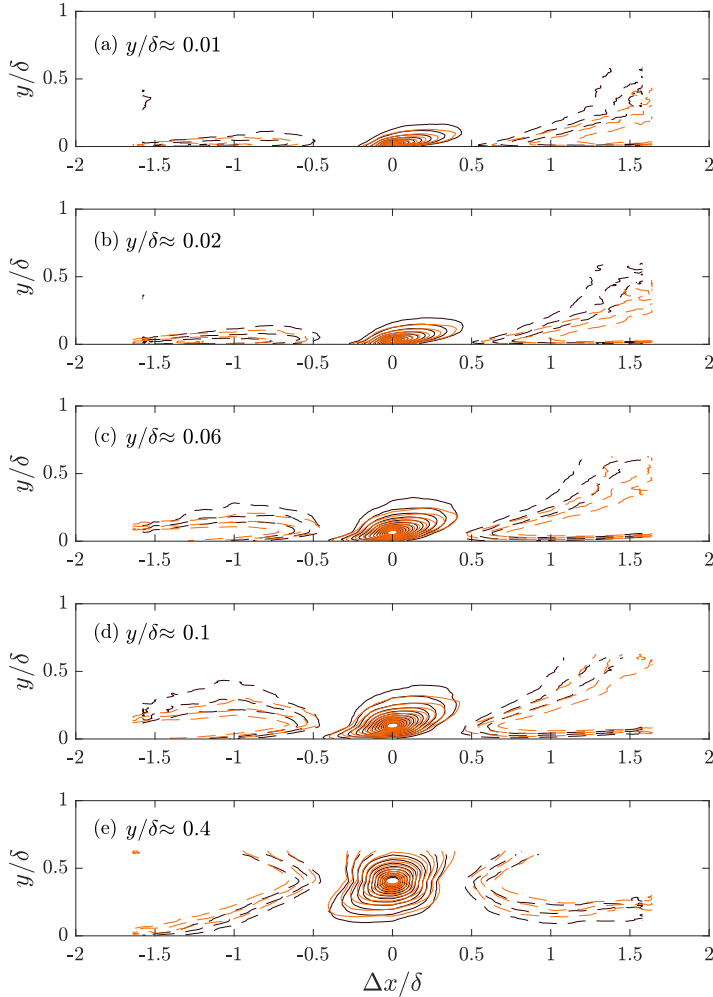


FIG. 14. R_{iii} correlation computed at different wall-normal locations. (a) $y^+ \approx 55$ ($y/\delta \approx 0.01$), (b) $y^+ \approx 100$ ($y/\delta \approx 0.02$), (c) $y^+ \approx 320$ ($y/\delta \approx 0.065$), (d) $y^+ \approx 500$ ($y/\delta \approx 0.1$), (e) $y/\delta \approx 0.4$. Orange line: case B, black line: Case D. Negative contours are shown with dashed lines. The outermost contour level and the increment are 0.1 and 0.05 for positive contours, respectively, and -0.1 and -0.05 for negative contours, respectively. Zero contours are not shown.

positive correlations have inclined features which will be discussed in more detail in the following paragraphs.

The single iso-contour (at level of 0.25) is shown in Fig. 15 for the two cases of FST at several wall-normal locations as illustrated for Fig. 14. There is very little difference in the extent and shape of the structures between the two cases. Even the way these structures are inclined seem to be similar for both cases. This inclined feature of the structures is compared with two canonical cases (where data are available): one is from the PIV measurements of Gomit *et al.* [41] for a turbulent boundary layer developing over a flat plate at $Re_\tau \approx 4000$, and the second is from the canonical case for the same setup of the present study in the absence of the active grid with $Re_\tau \approx 1100$. For Gomit *et al.* [41], the nearest wall correlations can be obtained above $y/\delta \approx 0.06$. It is remarkable how the structures are inclined similarly. This suggests that the addition of free-stream turbulence and also the change in its turbulence level do not affect the structural organization of the flow

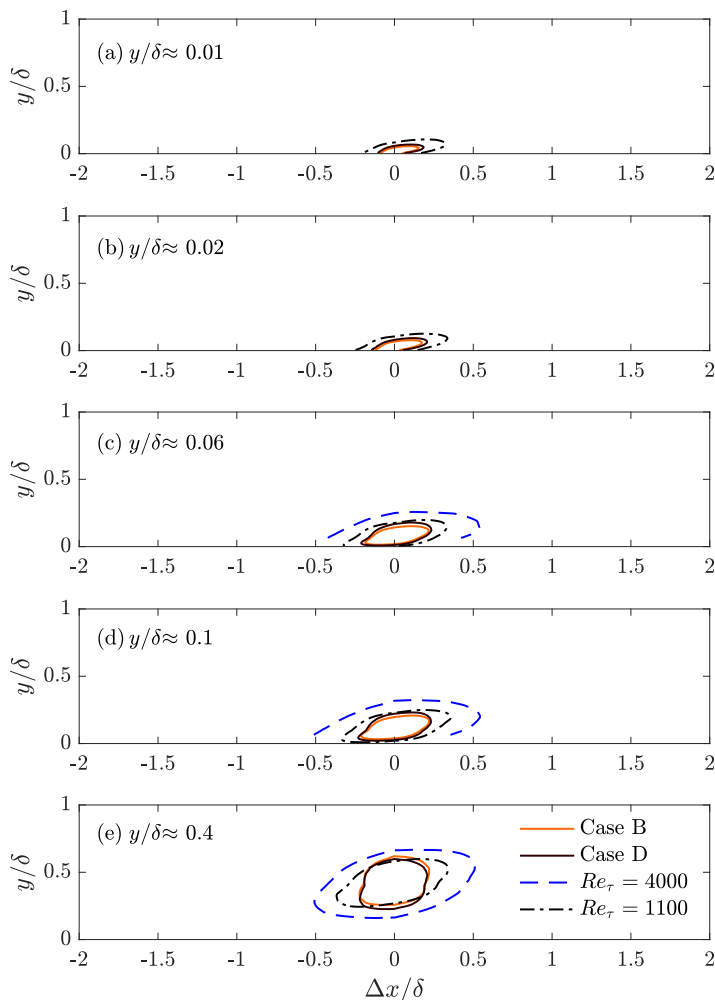


FIG. 15. R_{ii} correlation comparison for FST cases at different wall-normal locations as indicated on the plots. Representative contour level is 0.25. Canonical cases from the literature are included (where data are available) for comparison. Dashed line: $Re_\tau = 4000$ from Gomit *et al.* [41], dot-dashed line: $Re_\tau = 1100$ from the present study case without FST.

in the streamwise-wall-normal plane. This finding, when interpreted together with the observed structural similarity of flow over rough walls [42–44], suggests that a universal structural similarity may be present. The structure observed in Fig. 15 does not seem to depend on the FST boundary condition. This is remarkable since the extent of disturbance in this case is over 10% (in FST level), which is stronger than the near-wall peak turbulence intensity in a comparable Reynolds number canonical flow. The extent of the correlations is shorter for FST cases as would be expected since the penetrated FST scales are less correlated in the boundary layer. Also due to these penetrated scales in the wall-normal direction, the shape of the correlations in the outer region is more rounded for FST cases. It is also worth mentioning the difference in Re_τ between FST and canonical cases for the same setup (with and without the active grid). The increase in Re_τ is achieved with increased FST by the active grid, which was previously noted by Dogan *et al.* [6] as an enhancement to small-scale facilities.

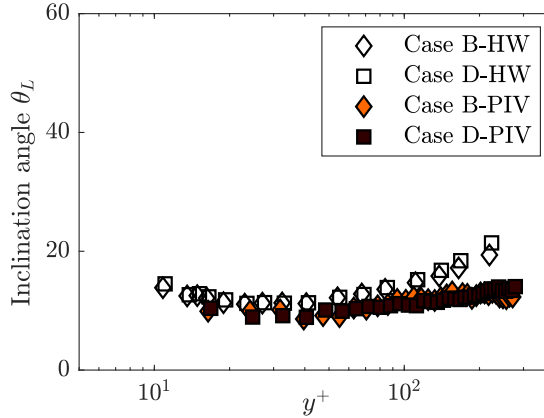


FIG. 16. Comparison of the inclination angle, θ_L , obtained through hot-wire and PIV measurements. Symbols are explained in the legend.

It is well established in the literature that the outer layer of a canonical boundary layer contains inclined structures that are associated with ejections and sweeps [45,46]. Adrian *et al.* [47] referred to these structures, which are coherently aligned in the streamwise direction creating a large-scale coherent motion, as hairpin vortex packets. The model of Adrian *et al.* [47] supported the existence of vortex organization in both the near-wall and outer layer of the flow. One of the characteristic feature of these packets is the streamwise alignment of a series of hairpin vortices, inclined away from the wall at angles between 12° and 20° [48]. However, the present study is not focused on the specific coherent structures that create this organization. Here the structural organization underlying the correlation contours will be presented. For this purpose, the inclination angle can be estimated from the correlation contours by assuming an elliptical shape for a constant contour level and determining the angle of the major axis of the fitted ellipse. The variation of this angle across the boundary layer is shown in Fig. 16. In addition, the results obtained from the multipoint measurements using a rake of hot-wire probes performed for the same cases (see Dogan *et al.* [6]), are also included in Fig. 16 for comparison. The angle from the multipoint hot-wire measurements is computed using the streamwise shift between the inner and outer probe signals by implementing Taylor's hypothesis. The results from these two methods (note that the PIV wall-normal extent is limited compared to the available measurement range of multiwire measurements) are comparable. The discrepancy in the outer most region may be related to the difference in analysis methodology given that Taylor's hypothesis was applied for the analysis of the hot-wire data. Nonetheless, the inclination angle of the structures is found to be consistent with the literature and, to reiterate, suggests promising results for the analogy between high-Reynolds-number flows and the present study cases as the structural organization inside the boundary layer is not altered despite the external disturbance from FST.

Figure 17 shows R_{uu} , R_{vv} , and R_{uv} correlations at two representative wall-normal locations for the two FST cases in comparison. For the two FST cases the correlations are comparable, which may be expected given the similarity of the shape and extent of the two-point autocorrelations shown previously in Figs. 14 and 15. The sharp drop of R_{vv} correlation at $y/\delta \approx 0.06$ is noteworthy, which suggests that the streamwise coherence of the v fluctuations is comparatively short. In the outer region, $y/\delta \approx 0.4$, the streamwise extent increases due to higher interactions with the free stream and the direct penetration of FST into the boundary layer in this region, hence the increased v fluctuations. R_{uv} correlations at $y/\delta \approx 0.06$, similar to R_{uu} , have long streamwise coherence. The negative values suggest that the low-speed fluid is associated with an upwash over long streamwise distances [39]. Comparing the correlations for positive and negatives values of $\Delta x/\delta$, there is a slight asymmetry that is more pronounced for the data given at $y \approx 0.4$ in the outer region of the

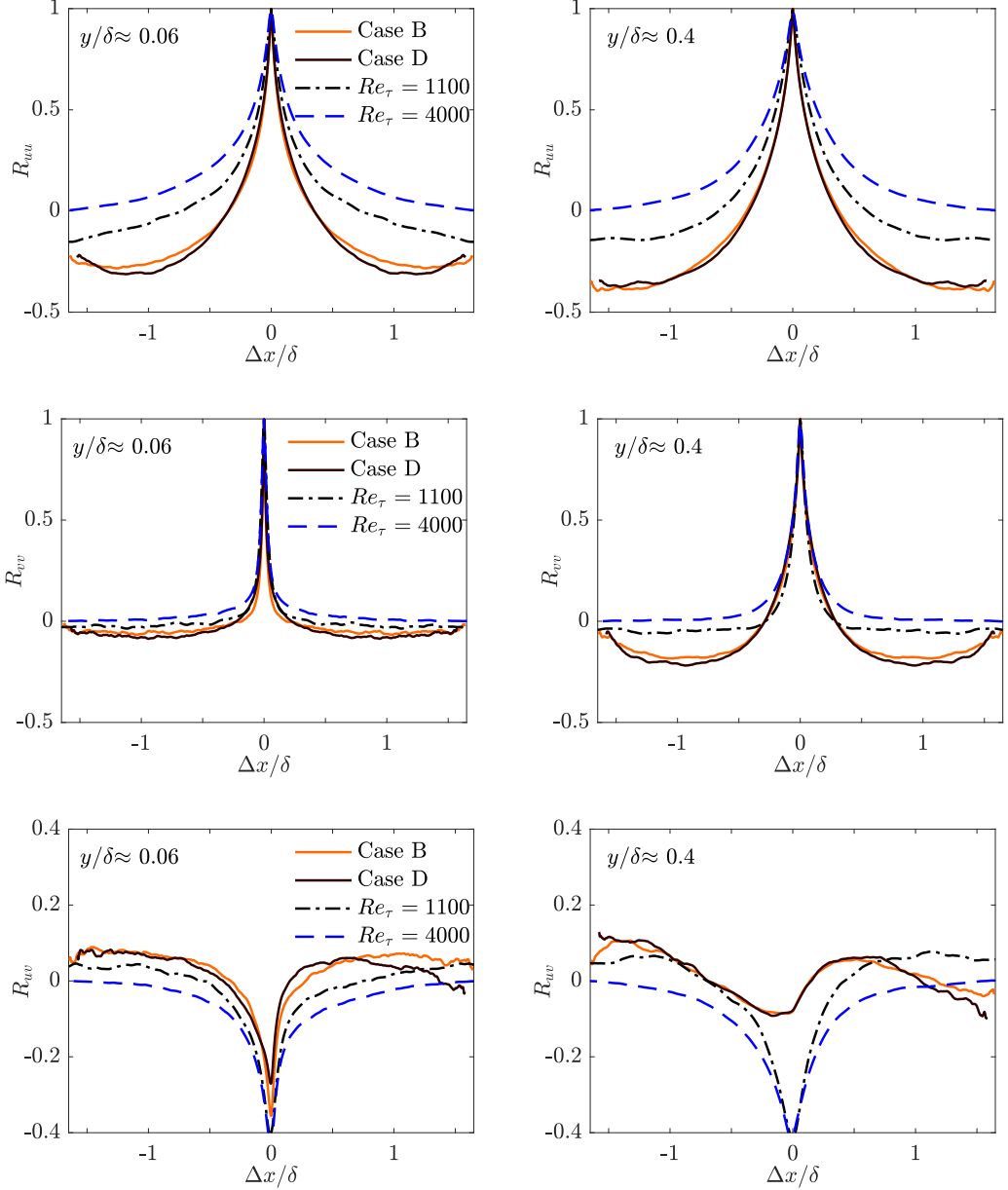


FIG. 17. (Top) R_{uu} , (middle) R_{vv} , and (bottom) R_{uv} correlations at (left) $y/\delta \approx 0.06$ and (right) $y/\delta \approx 0.4$ for both FST cases in comparison with the canonical cases from the literature. Dashed line: $Re_\tau = 4000$ from Gomit *et al.* [41], dot-dashed line: $Re_\tau = 1100$ from the present study case without FST.

boundary layer. In addition to the FST cases, the same canonical boundary layer data that were included previously in Fig. 15 are shown for comparison to the correlations in Fig. 17. Similarly, it is observed that the extent of the correlations is larger for canonical cases. The negative correlations are mostly encountered for FST cases and more so in the outer region due to the penetration of FST scales into the boundary layer.

Length scales in the wall-normal and free-stream direction are estimated from the corresponding extent of the R_{uu} and R_{vv} contours at a specified level, as was previously done by Christensen and

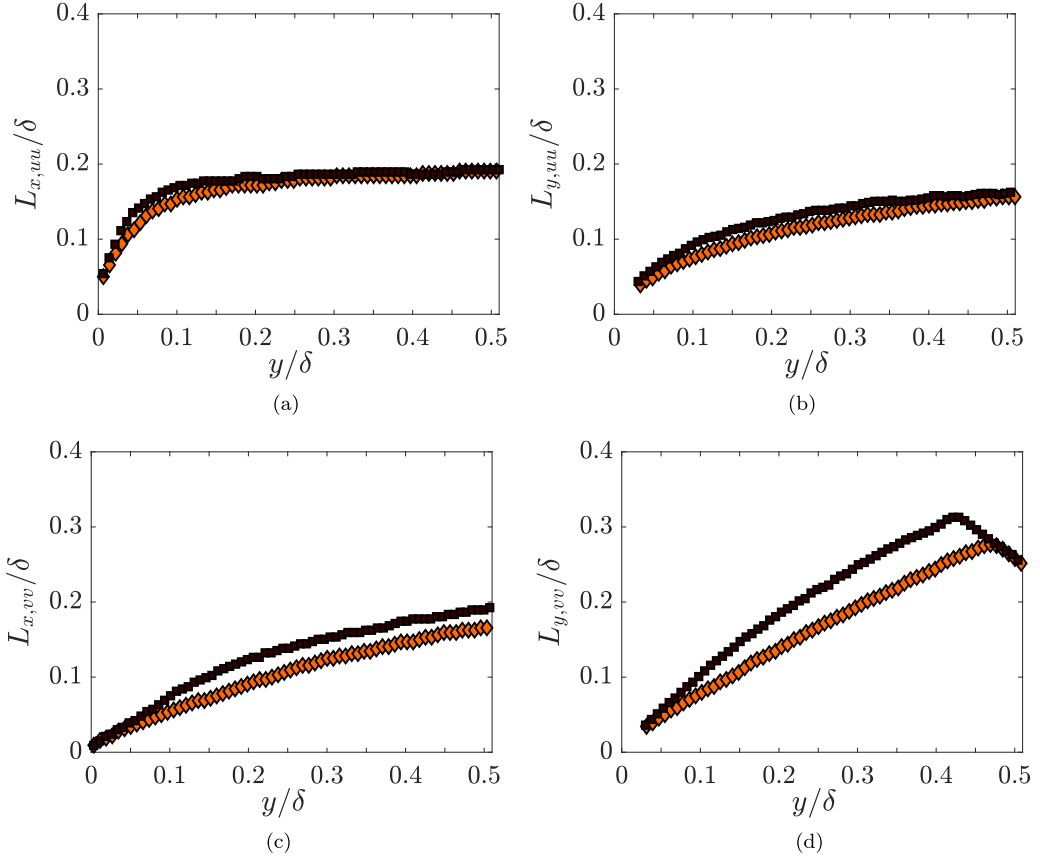


FIG. 18. Wall-normal variation of (a), (c) streamwise and (b), (d) wall-normal length scales based on $R_{uu} = 0.5$ and $R_{vv} = 0.5$ for both FST cases. Case B: filled diamond, case D: filled square.

Wu [49]. Figure 18 shows these length scales for both FST cases as determined using the streamwise and wall-normal extent of R_{uu} and R_{vv} for a contour level of 0.5. It should be noted that the wall-normal length scales are presented for $y/\delta \geq 0.03$ as; below this location, the contours begin to merge with the wall, and therefore it is difficult to apply a similar analysis of the wall-normal extent. Since the calculated length scales depend on the chosen contour level, these plots will only reveal the trends of the length scales in the boundary layer. L_x of R_{uu} correlations seem to stay constant for both cases for the wall-normal range presented. The aforementioned trend is similar to that of a channel flow [49]. The L_y determined from the R_{uu} correlations are similar in magnitude for the two cases; however, L_y exhibits a gradual increase beyond the log region.

L_y of R_{uu} correlations almost collapse for two cases and show a gradual increase above the log region. It should be noted that the wall-normal length scales are presented for $y/\delta \geq 0.03$ as, below this location, the contours begin to merge with the wall, and therefore it is difficult to apply a similar analysis of the wall-normal extent. For L_x of R_{vv} , as shown in Fig. 18, the length scales appear to approach a near-zero value at the wall, owing to the low streamwise coherence of R_{vv} as was previously noted. For these length scales, the high-turbulence case D has slightly higher values than the low-turbulence case B above $y/\delta \approx 0.1$ throughout the range shown. This could be justified by different penetration levels of these two cases, as an increased penetration of FST would be associated with higher wall-normal fluctuations in the boundary layer. A decrease of L_y above $y/\delta \approx 0.4$ for case D and above $y/\delta \approx 0.45$ for case B is shown in Fig. 18. The observed decrease may be attributed to the uncorrelated free-stream fluctuations that were found to dominate in these regions

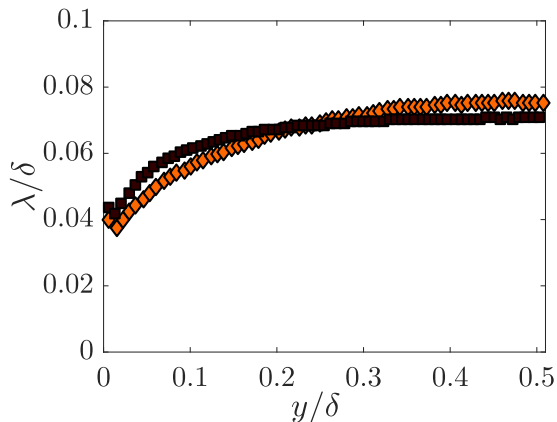


FIG. 19. Wall-normal variation of Taylor microscale for both FST cases. Case B: filled diamond, case D: filled square.

due to the direct penetration of FST (e.g., as shown in Fig. 4). In addition to the correlation length scales, it might be instructive to present Taylor microscale variation across the boundary layer. Taylor microscale, λ , is calculated as $\sqrt{(15\nu\overline{u'^2})/\epsilon}$. Within this definition, the turbulence energy dissipation rate, ϵ , is calculated from the spatial gradient of the streamwise velocity fluctuations as $15\nu(\partial u/\partial x)^2$. Figure 19 shows the Taylor microscale wall-normal variation in outer scaling for both FST cases. There is an increasing trend near the wall until close to the edge of the logarithmic region ($y/\delta \approx 0.2$) for both cases with the penetration of large scales into the boundary layer. In line with the boundary layer growth due to the external disturbance, this increasing trend slows and stays almost constant.

VI. CONCLUSION

The present experimental study includes a detailed account of the response of the turbulent boundary layer to high levels of free-stream turbulence from the perspective of statistical and structural information obtained using a planar PIV measurement technique. This study therefore builds upon the related work of Dogan *et al.* [5,6]. It is shown that wall-normal velocity and Reynolds shear stress profiles followed the inner scaling, which has been found contrary to the streamwise fluctuations. The streamwise fluctuations exhibited an outer peak that grows in amplitude with increasing FST level, which is also a remarkably similar feature of high-Reynolds-number canonical flows. As for the Reynolds shear stress profiles, the plateau region observed around the local peak is broadened for increasing FST level, which is similarly observed in high-Reynolds-number wall-bounded flows as Re_τ increases.

Quadrant analysis was employed to determine the contributions of different Reynolds-stress-producing events. The dominant contributors were found to be sweep and ejection events in the boundary layer. The outward and inward interaction events were observed to contribute more towards the edge of the boundary layer. These results suggest a degree of similarity in momentum transport between the present cases and channel flows. The common intermittency characteristics of the two flows is believed to play the main role in this similarity. The effect of this common feature was also observed for both flows in the mean streamwise velocity profiles at the outermost region of the boundary layer.

The structural organization of the flow was presented using two-point spatial velocity correlations. This enabled describing the coherence of the turbulent structures in the boundary layer. The streamwise velocity autocorrelations showed structures that are coherent for extended distances in

streamwise direction, whereas the wall-normal velocity correlations were found to be quite short in streamwise coherence. The inclination angle of these coherent structures was estimated using the correlation contours, and the value was found to be consistent with the literature for canonical cases. This similarity implies that the structural organization inside the boundary layer was not altered despite the external disturbance from FST. This signifies a potential universal structural representation of wall-bounded flows where the boundary conditions do not change the organization of the structures but their strength.

ACKNOWLEDGMENTS

The authors acknowledge the financial support of the European Research Council (ERC Grant Agreement No. 277472), and the Engineering and Physical Sciences Research Council of the United Kingdom (EPSRC Grant Ref. No. EP/L006383/1). R.J.H. was partially funded by the Natural Sciences and Engineering Research Council of Canada (NSERC) while at the University of Southampton and is presently supported by the Onsager Fellowship program at NTNU. E.D. was partially funded by Zonta International while at the University of Southampton and was funded at KTH by the Wallenberg Foundation (within the Wallenberg Academy Fellow program for Philipp Schlatter).

-
- [1] M. F. Blair, Influence of free-stream turbulence on turbulent boundary layer heat transfer and mean profile development, part I—Experimental data, *J. Heat Transfer* **105**, 33 (1983).
 - [2] P. E. Hancock and P. Bradshaw, The effect of free-stream turbulence on turbulent boundary layers, *J. Fluids Eng.* **105**, 284 (1983).
 - [3] J. C. R. Hunt, P. A. Durbin, and X. Wu, *Interactions between freestream turbulence and boundary layers*, Tech. Rep. (Center for Turbulence Research, Stanford, California, 1998).
 - [4] N. S. Sharp, S. Neuscamman, and Z. Warhaft, Effects of large-scale free stream turbulence on a turbulent boundary layer, *Phys. Fluids* **21**, 095105 (2009).
 - [5] E. Dogan, R. E. Hanson, and B. Ganapathisubramani, Interactions of large-scale free-stream turbulence with turbulent boundary layers, *J. Fluid Mech.* **802**, 79 (2016).
 - [6] E. Dogan, R. J. Hearst, and B. Ganapathisubramani, Modelling high Reynolds number wall-turbulence interactions in laboratory experiments using large-scale free-stream turbulence, *Philos. Trans. R. Soc. A* **375**, 20160091 (2017).
 - [7] B. Ganapathisubramani, E. K. Longmire, and I. Marusic, Characteristics of vortex packets in turbulent boundary layers, *J. Fluid Mech.* **478**, 35 (2003).
 - [8] M. Guala, S. E. Hommema, and R. J. Adrian, Large-scale and very-large-scale motions in turbulent pipe flow, *J. Fluid Mech.* **554**, 521 (2006).
 - [9] B. J. Balakumar and R. J. Adrian, Large- and very-large-scale motions in channel and boundary-layer flows, *Philos. Trans. R. Soc. A* **365**, 665 (2007).
 - [10] P. E. Hancock and P. Bradshaw, Turbulence structure of a boundary layer beneath a turbulent free stream, *J. Fluid Mech.* **205**, 45 (1989).
 - [11] B. Stefes and H.-H. Fernholz, Skin friction and turbulence measurements in a boundary layer with zero-pressure-gradient under the influence of high intensity free-stream turbulence, *Eur. J. Mech. B* **23**, 303 (2004).
 - [12] K. A. Thole and D. G. Bogard, High freestream turbulence effects on turbulent boundary layers, *J. Fluids Eng.* **118**, 276 (1996).
 - [13] H. Makita, Realization of a large-scale turbulence field in a small wind tunnel, *Fluid Dyn. Res.* **8**, 53 (1991).
 - [14] K. T. Christensen, The influence of peak-locking errors on turbulence statistics computed from PIV ensembles, *Exp. Fluids* **36**, 484 (2004).
 - [15] R. J. Hearst and B. Ganapathisubramani, Quantification and adjustment of pixel-locking in particle image velocimetry, *Exp. Fluids* **56**, 1 (2015).

- [16] J. V. Larssen and W. J. Devenport, On the generation of large-scale homogeneous turbulence, *Exp. Fluids* **50**, 1207 (2011).
- [17] R. J. Hearst and P. Lavoie, The effect of active grid initial conditions on high Reynolds number turbulence, *Exp. Fluids* **56**, 185 (2015).
- [18] L. B. Esteban, E. Dogan, E. Rodríguez-López, and B. Ganapathisubramani, Skin-friction measurements in a turbulent boundary layer under the influence of free-stream turbulence, *Exp. Fluids* **58**, 115 (2017).
- [19] N. Hutchins and I. Marusic, Large-scale influences in near-wall turbulence, *Philos. Trans. R. Soc. A* **365**, 647 (2007).
- [20] K. M. Talluru, R. Baidya, N. Hutchins, and I. Marusic, Amplitude modulation of all three velocity components in turbulent boundary layers, *J. Fluid Mech.* **746**, R1 (2014).
- [21] M. Lee and R. D. Moser, Direct numerical simulation of turbulent channel flow up to $Re_\tau \approx 5200$, *J. Fluid Mech.* **774**, 395 (2015).
- [22] A. E. Perry and J. D. Li, Experimental support for the attached-eddy hypothesis in zero-pressure-gradient turbulent boundary layers, *J. Fluid Mech.* **218**, 405 (1990).
- [23] T. Wei and J. Klewicki, Scaling properties of the mean wall-normal velocity in zero-pressure-gradient boundary layers, *Phys. Rev. Fluids* **1**, 082401 (2016).
- [24] A. Lozano-Durán and J. Jiménez, Effect of the computational domain on direct simulations of turbulent channels up to $Re_\tau = 4200$, *Phys. Fluids* **26**, 011702 (2014).
- [25] D. B. De Graaff and J. K. Eaton, Reynolds-number scaling of the flat-plate turbulent boundary layer, *J. Fluid Mech.* **422**, 319 (2000).
- [26] M. H. Buschmann and M. Gad-el Hak, Normal and cross-flow Reynolds stresses: Differences between confined and semi-confined flows, *Exp. Fluids* **49**, 213 (2010).
- [27] R. Örlü, T. Fiorini, A. Segalini, G. Bellani, A. Talamelli, and P. H. Alfredsson, Reynolds stress scaling in pipe flow turbulence—First results from CICLOPE, *Philos. Trans. R. Soc. A* **375**, 20160187 (2017).
- [28] H. S. Kang, S. Chester, and C. Meneveau, Decaying turbulence in an active-grid-generated flow and comparisons with large-eddy simulation, *J. Fluid Mech.* **480**, 129 (2003).
- [29] P. J. A. Priyadarshana and J. C. Klewicki, Study of the motions contributing to the Reynolds stress in high and low Reynolds number turbulent boundary layers, *Phys. Fluids* **16**, 4586 (2004).
- [30] E. R. Corino and R. S. Brodkey, A visual investigation of the wall region in turbulent flow, *J. Fluid Mech.* **37**, 1 (1969).
- [31] J. M. Wallace, H. Eckelmann, and R. S. Brodkey, The wall region in turbulent shear flow, *J. Fluid Mech.* **54**, 39 (1972).
- [32] S. S. Lu and W. W. Willmarth, Measurements of the structure of the Reynolds stress in a turbulent boundary layer, *J. Fluid Mech.* **60**, 481 (1973).
- [33] R. J. Adrian, Hairpin vortex organization in wall turbulence, *Phys. Fluids* **19**, 041301 (2007).
- [34] J. Jiménez, S. Hoyas, M. P. Simens, and Y. Mizuno, Turbulent boundary layers and channels at moderate Reynolds numbers, *J. Fluid Mech.* **657**, 335 (2010).
- [35] W. W. Willmarth and S. S. Lu, Structure of the Reynolds stress near the wall, *J. Fluid Mech.* **55**, 65 (1972).
- [36] D. G. Bogard and W. G. Tiederman, Burst detection with single-point velocity measurements, *J. Fluid Mech.* **162**, 389 (1986).
- [37] A. Lozano-Durán, O. Flores, and J. Jiménez, The three-dimensional structure of momentum transfer in turbulent channels, *J. Fluid Mech.* **694**, 100 (2012).
- [38] J. M. Wallace, Space-time correlations in turbulent flow: A review, *Theor. Appl. Mech. Lett.* **4**, 022003 (2014).
- [39] B. Ganapathisubramani, N. Hutchins, W. T. Hambleton, E. K. Longmire, and I. Marusic, Investigation of large-scale coherence in a turbulent boundary layer using two-point correlations, *J. Fluid Mech.* **524**, 57 (2005).
- [40] M. Tutkun, W. K. George, J. Delville, M. Stanislas, P. B. V. Johansson, J.-M. Foucaut, and S. Coudert, Two-point correlations in high Reynolds number flat plate turbulent boundary layers, *J. Turbul.* **10**, N21 (2009).
- [41] G. Gomit, R. de Kat, and B. Ganapathisubramani, Structure of high and low shear-stress events in a turbulent boundary layer, *Phys. Rev. Fluids* **3**, 014609 (2018).

- [42] J. Jiménez, Turbulent flows over rough walls, *Annu. Rev. Fluid Mech.* **36**, 173 (2004).
- [43] K. A. Flack, M. P. Schultz, and T. A. Shapiro, Experimental support for Townsend's Reynolds number similarity hypothesis on rough walls, *Phys. Fluids* **17**, 035102 (2005).
- [44] M. Placidi, On the effect of surface morphology on wall turbulence, Ph.D. thesis, University of Southampton (2015).
- [45] G. L. Brown and A. S. W. Thomas, Large structure in a turbulent boundary layer, *Phys. Fluids* **20**, S243 (1977).
- [46] M. R. Head and P. Bandyopadhyay, New aspects of turbulent boundary-layer structure, *J. Fluid Mech.* **107**, 297 (1981).
- [47] R. J. Adrian, C. D. Meinhart, and C. D. Tomkins, Vortex organization in the outer region of the turbulent boundary layer, *J. Fluid Mech.* **422**, 1 (2000).
- [48] K. T. Christensen and J. R. Adrian, Statistical evidence of hairpin vortex packets in wall turbulence, *J. Fluid Mech.* **431**, 433 (2001).
- [49] K. T. Christensen and Y. Wu, Characteristics of vortex organization in the outer layer of wall turbulence, in *TSFP Digital Library Online* (Begel House, 2005).